Catalysts **2014**, *4*, 196-214; doi:10.3390/catal4020196

OPEN ACCESS

catalysts

ISSN 2073-4344

www.mdpi.com/journal/catalysts

Review

Deactivation Pattern of a "Model" Ni/MgO Catalyst in the Pre-Reforming of *n*-Hexane †

Giuseppe Trunfio [1] **and Francesco Arena** [1,2,*]

[1] Dipartimento di Ingegneria Elettronica, Chimica e Ingegneria Industriale, Università degli Studi di Messina, Viale F. Stagno D'Alcontres 31, I-98166 Messina, Italy; E-Mail: gtrunfio@unime.it

[2] Istituto CNR-ITAE "Nicola Giordano", Salita S. Lucia 5, I-98126 Messina, Italy

† Dedicated to Professor Adolfo Parmaliana, who died five years ago (2 October 2008), for his passionate contribution to the research topic of hydrocarbon reforming.

* Author to whom correspondence should be addressed; E-Mail: Francesco.Arena@unime.it; Tel.: +39-90-676-5606; Fax: +39-90-391518.

Received: 14 August 2013; in revised form: 20 January 2014 / Accepted: 5 June 2014 / Published: 19 June 2014

Abstract: The deactivation pattern of a "model" Ni/MgO catalyst in the pre-reforming of *n*-hexane with steam (*T*, 450 °C; *P*, 5–15 bar) is reviewed. The influence of the steam-to-carbon ratio (S/C, 1.5–3.5) on the rate of catalyst fouling by coking is ascertained. Catalyst fouling leads to an exponential decay in activity, denoting 1st-order dependence of the coking process on active sites availability. Hydrogen hinders the coking process, though slight activity decay is due to sintering of the active Ni phase. Deactivation by thiophene causes a sharp, almost linear, drop to nearly zero activity within only 6 h; this deactivation is likely due to dissociative adsorption of thiophene with subsequent strong, irreversible chemical adsorption of S-atoms on active Ni sites, *i.e.*, irreversible poisoning. Modeling of activity decay curves (α, a_t/a_0) by proper kinetic equations allows assessing the effects of temperature, pressure, S/C, H_2 and thiophene feed on the deactivation pattern of the model Ni/MgO catalyst by coking, sintering, and poisoning phenomena.

Keywords: pre-reforming; activity decay; poisoning; sintering

---

1. Introduction

There is a strong commitment worldwide to enhance the practical and economical feasibility of the steam reforming (SR) technology through efficiency improvement and feedstock versatility, which could result in significant improvements in fuel processing economy [1–7]. In this context, pre-reforming constitutes an established technology with economic and operational benefits on the overall syngas production, representing an important tool, especially for the revamping of older SR plants [2–4,8–10]. A pre-reforming unit consists in a tubular adiabatic reformer, allowing whatever hydrocarbon feed (NG, LPG, VN) be converted to CH_4 and CO_x at low temperature, typically in the 450–550 °C range, with many practical advantages consisting of [2–4]:

i. an increased production capacity with smaller reformer furnaces;
ii. a higher feedstock flexibility;
iii. enhanced SR tube and catalyst lifetime;
iv. design of innovative process configuration for low energy consumption and investment costs.

Furthermore, the pre-reforming unit drastically limits the risk of carbon formation inside tubular reformers, ensuring a total conversion of higher hydrocarbons, and allowing, then, SR operations at lower steam-to-carbon (S/C) ratio, with a higher preheat temperature and heat flux and capacity [9–11]. Moreover, the pre-reforming catalyst ensures the total elimination of S-containing impurities, contributing to enhance SR catalysts' lifetime [2–5,8,11–14].

Considering the importance for the improvement of syngas producing plants, little previous literature deals with the basic aspects of the steam reforming of higher hydrocarbons reaction under low temperature and high pressure conditions [12,14–17]. In fact, only after the pioneering work of Rostrup-Nielsen on the steam reforming of C1-C7 alkanes on magnesia-supported metal catalysts, which led to the development of the SPARG process [2,10,14], has light been shed on the reaction mechanism and kinetics, leading to further improvements in catalysts' performance [11,14,16,17].

Although noble-metal-based systems feature a high reactivity in the reforming of superior hydrocarbons to methane and carbon oxides, typical formulations of pre-reforming catalysts include nickel as the active phase [6–8,16,17]. Due to different operating conditions, pre-reforming catalysts are generally richer in Ni loading (50–70 wt%), with the addition of rare earth elements (e.g., La, Sm, Ce, Y, Zr, *etc.*) as promoters, and are characterized by larger total (SA) and metal surface area (MSA) than SR counterparts [6,16]. Loading of the active phase and type of promoters, however, depend upon process characteristics and targets [6,16].

Generally, coking processes on Ni-based catalysts in steam reforming and methanation reactions proceed through common carbon intermediates leading to the formation of several types of deposits depending on operating conditions [2,8,12–15,18–24]. Moreover, effects of metal sintering on the active surface area of typical pre-reforming catalysts have been assessed [25]. Catalyst poisoning is generally caused by strong chemisorption of sulfur impurities present in the feed stream as inorganic and/or organic sulfides in most naturally occurring feedstock; sulfur poisoning depends on many variables including the kind of sulfur compound, nature of the catalyst and operating conditions [7,26,27].

In earlier papers, we documented that Ni/MgO catalysts obtained by an original non-aqueous preparation route exhibit a remarkable performance in both "steam" and "dry" reforming of

methane [28–30]. Hindering the formation of the $NiMgO_x$ solid solution, indeed, such a preparation procedure allows tuning both physico-chemical and catalytic properties through a proper selection of Ni loading, calcination and reduction treatments [28,29,31].

This review provides an overview of reaction and deactivation networks occurring early (*i.e.*, during the first 17 h) on a "model" Ni/MgO catalyst in the steam reforming of *n*-hexane under pre-reforming conditions (*T*, 450 °C; *P*, 5–15 atm). Rates, selectivities, rate constants, and equilibrium constants of important reaction paths as a function of time and rate constants for deactivation by sintering, coking, and poisoning from the previous literature (with an emphasis on the authors' previous works) are presented, and the effects of catalyst deactivation on activity, selectivity, and stability are analyzed and discussed.

2. Results and Discussion

2.1. Effects of the Experimental Conditions on the Activity-Selectivity-Stability Pattern

Activity data of the "model" Ni/MgO catalyst in the pre-reforming of *n*-hexane at standard reaction conditions (*T*, 450 °C; *P*, 10 bar; P_{C6H14}, 0.18 bar; P_{H2O}, 3.0 bar; S/C, 2.8) are shown in Figure 1 in terms of n-hexane conversion (χ) and product selectivity *vs.* reaction time (t.o.s.). The only detected products are CH_4, CO_2, and CO [11–17] with a relative distribution which depends on the conversion level. After 30 min, taken as the initial reaction time (t_0, a_0), the hexane conversion is ≈70% with CH_4, CO_2 and CO selectivities of *ca.* 55, 43 and 2%, respectively. A drop in conversion of about 50% over a period of only 17 h involves a S_{CH4} decrease from 55 to 30%, counterbalanced by a rise in S_{CO2} from 45 to 70%, although no significant changes in S_{CO} (2–3%) are observed.

Figure 1. n-hexane conversion (χ) and product selectivity (Sχ) *vs.* t.o.s. at standard reaction conditions (adapted from ref. [11] with the kind permission of Elsevier, copyright 2004).

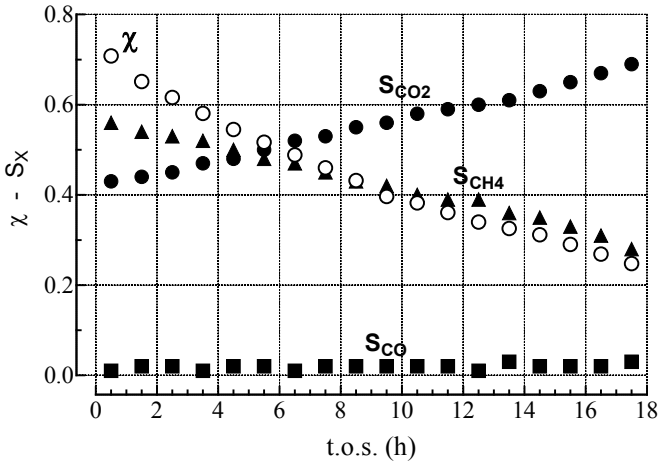

Activity data at 450 °C with varying space velocity (GHSV), feed stream composition (P_{H2O} and P_{H2}) and pressure are summarized in Table 1 in terms of initial and final hexane conversion (χ, %), reactor output ($mol_{C6H14} \cdot h^{-1} \cdot g_{cat}^{-1}$), product selectivity ($S_\chi$, %) and weight gain of the "used" catalyst samples (W_C, gg_{cat}^{-1}) due to carbon deposition and/or coke formation, determined by TGA-DSC

measurements. In addition, the influence of experimental conditions on the "relative activity" ($\alpha = \chi/\chi_0$, the ratio between conversion at the time "t" and "t_0" respectively) is shown in Figure 2.

Table 1. Initial and final (17 h) activity data and amount of carbon on the "used" catalyst samples under different reaction conditions (T, 450 °C; p_{C6H14}/p^0, 0.018).

Run	P (atm)	S/C	GHSV [a] (h^{-1})	χ_{C6H14} (%)	Reactor output ($mol_{C6H14}\ h^{-1}\ g_{cat}^{-1}$)	S_{CH4} (%)	S_{CO2} (%)	S_{CO} (%)	S_{C2-C5} (%)	W_C [b] ($g\ g_{cat}^{-1}$)
a	10	1.5	12,000	53–08	0.26 – 0.04	55–9	43–88	2–3	-	1.32
b	10	2.8	12,000	71–25	0.35–0.12	56–28	42–69	2–3	-	0.96
c	10	3.5	12,000	76–34	0.38–0.17	56–42	43–57	1–1	-	0.89
d	10	2.8	24,000	38–11	0.38–0.11	39–5	59–93	2–2	-	1.23
e [c]	10	2.8	24,000	77–73	0.77–0.73	98–97	1–2	0–0	1–1	0.03
f	15	2.8	12,000	69–37	0.51–0.27	60–50	39–49	1–1	-	0.75
g	5	2.8	12,000	67–21	0.17–0.05	49–25	49–73	1–2	-	1.02
h [d]	10	2.8	24,000	65–00	0.65–0.00	97–97	2–2	1–1	-	0.21

[a] F_{C6H14}/V_{cat}; [b] weight gain due to carbon deposition and/or coke formation; [c] hydrogen (H_2/C, 1) in the feed; [d] hydrogen (H_2/C, 1) and thiophene (50 ppm on C_6H_{14}) in the feed.

Data in Table 1 indicate that feed composition and operating conditions affect both hexane conversion and CH_4, CO_2 and CO selectivities, while trace amounts of C2-C5 hydrocarbons ($S_{C2-C5} \approx$ 1%) are detected only in presence of hydrogen (run e).

Figure 2. Relative activity *vs.* t.o.s. at different experimental conditions (see Table 1).

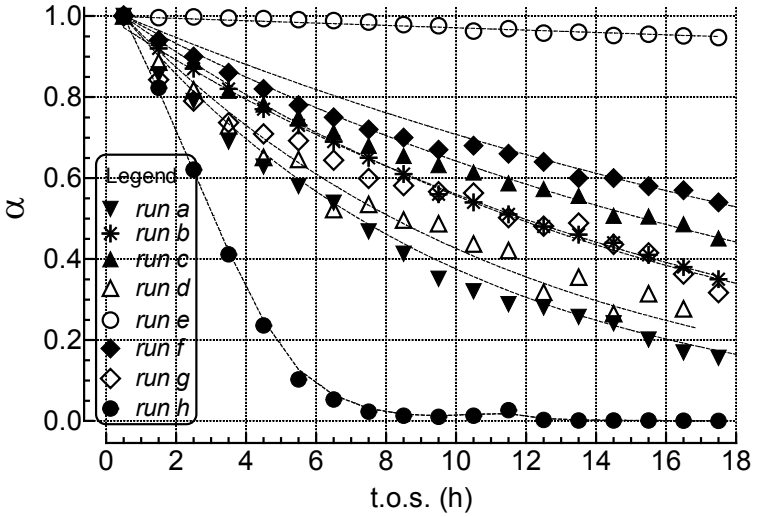

At a constant pressure of 10 atm, the most obvious effects of the S/C ratio increase from 1.5 to 3.5 (runs a–c) consist in a progressive increase of hexane conversion (from 53 to 76%), indicating a positive effect of water pressure on the reactor output, and a better catalyst stability (Figure 2) coupled to a relative influence on product selectivity during reaction time (Table 1). The pressure increase from 5 to 15 atm (S/C, 2.8) has no significant effect on the conversion level (runs b, f, g), as an increase from 0.17 to 0.51 $mmol_{C6H14} \cdot h^{-1} \cdot g_{cat}^{-1}$ (Table 1) mirrors a fairly constant pressure-normalized reactor output (0.035 $mol_{C6H14} \cdot h^{-1} \cdot g_{cat}^{-1}$/atm).

Figure 3. Overall conversion-selectivity (S_χ) data and H/O_{out} ratio at different conditions (see Table 1) and reaction times (adapted from ref. [15] with the kind permission of Wiley, copyright 2006).

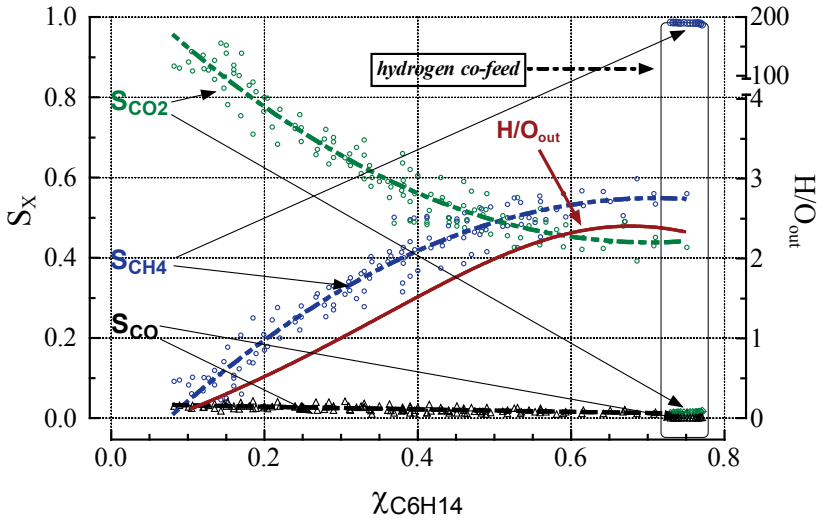

In addition, an enhancement of S_{CH4} (49–60%) and, even more so, of catalyst stability are evident, especially at 15 atm (run f).

Furthermore, a twofold increase of GHSV from 12,000 to 24,000 h^{-1} (runs b, d) causes an almost proportional decrease of the initial conversion (38%) according to an unchanging reactor output (0.35–0.38 $mol_{C6H14} \cdot h^{-1} \cdot g_{cat}^{-1}$), a drop in S_{CH4} from 55 to 39% with a corresponding growth of S_{CO2} (Table 1), and a considerably stronger activity decay (Figure 2).

In all the cases, a decreasing trend of the relative activity curves denotes noticeable deactivation phenomena, the extents of which depend on S/C ratio, P, and GHSV (Figure 2). The observed loss of activity can be largely accounted for by the weight loss recorded by TGA-DSC analysis of "used" catalyst samples (Table 1) during combustion of the carbonaceous deposits. This points to carbon formation and coking as the main causes of catalyst deactivation [11,15]. However, such experiments did not allow to differentiate between carbon and coke nor quantitatively measure CO_2 and H_2O.

Under simulated pre-reforming conditions (run e) with H_2 in the feed [3–6,16–18], a markedly higher initial conversion (77%) and a two-fold higher reactor output are observed relative to the standard tests (runs b, d). Moreover, the addition of hydrogen (H_2/C = 1) to the feed increases S_{CH4} to 97–98% and greatly improves catalyst stability, with only a minor *(ca.* 5%) activity loss during 17 h of t.o.s. (Figure 2, run e).

All the conversion-selectivity data at different conditions (see Table 1) and reaction times provide some general relationships showing that the selectivity pattern depends only on the activity level (Figure 3). Thus, S_{CH4} increases steadily with increasing conversion, reaching an asymptotic value of 55% in the conversion range of 60–80%, while S_{CO2} decreases from 90 to 45% and S_{CO} from 2 to 0.5% over the full range of measured conversion (8–75%). Changes in CO/CO_2 are consistent with the equilibrium composition predicted from the WGS reaction [11,15,16,18,19,32–37]. The overall result of these changes in product selectivities is a trend of increasing output hydrogen/oxygen atomic ratio (H/O_{out}) from zero at 8% conversion to a maximum value of 2.4 at 67% conversion (Figure 3), which is essentially the same as the H/C ratio of the hexane molecule of 2.33. The apparent increase in the

"hydrogenation" functionality with increasing conversion level is consistent with a reaction network involving (1) cracking of hexane; (2) water dissociation; (3) primary formation of CO, which is further transformed to CO_2 via the water-gas-shift (WGS); and (4) CH_4 via methanation (MET) paths respectively [11,15], according to the following surface reaction network, which includes two irreversible (1 and 8) and six reversible (2–7) steps [11,13–16,19,21,33,35].

CRK $$C_6H_{14} + n * \rightarrow (6 - m)\, C_{\alpha(s)} + m\, CH_{x(s)} + [(14 - x)/2]\, H_{2(g)} \quad (1)$$

WS $$H_2O + p * \overset{K_{WS}}{\leftrightarrows} H_{2(g)} + O_{(s)} \quad (2)$$

HC $$H_2 + 2 * \overset{K_{H2}}{\leftrightarrows} 2\, H_{(s)} \quad (3)$$

GAS $$C_{\alpha(s)} + O_{(s)} \overset{K_{GAS}}{\leftrightarrows} CO_{(s)} + (n/6 + m - q) * \quad (4)$$

MET $$C_{\alpha(s)} + 4\, H_{(s)} \overset{K_{MET}}{\leftrightarrows} CH_{4(g)} + (n/6 + 4 - t) * \quad (5)$$

WGS $$CO_{(s)} + O_{(s)} \overset{K_{WGS}}{\leftrightarrows} CO_{2(s)} + (m + q - s) * \quad (6)$$

DES $$CO_{2(s)} \overset{K_{CO2}}{\rightarrow} CO_{2(g)} + s * \quad (7)$$

COK $$z\, C_\alpha \overset{k_{COK}}{\rightarrow} C_\beta \text{ ("encapsulating" + "wiskers")} - w * \quad (8)$$

The above reaction scheme explains the inhibition of the methanation path (5) at low P_{CO} and P_{H2}, that is the case at low conversion, while the excess of steam favors the formation of CO_2 *via* the WGS path (6). Thus, hydrogen "availability", determined by the extent of hexane conversion, is the key-parameter controlling the CH_4/CO_2 distribution [38]. Therefore, enabling the gasification of coke-precursor species [11,15–17,21,22,35,36], the methanation step is the "competitor" process of coking, explaining the high catalyst stability and the negligible weight gain of the used catalysts under H_2 co-feeding (Table 1). In fact, the same carbon-intermediate (C_α) can undergo methanation at high H_2 concentrations or, at low H_2 concentrations, generate the following less reactive carbon species, precursors of C-deposit buildup [19–22,35,36], by ageing

- amorphous carbon (C_β),
- vermicular carbon (C_V),
- bulk Ni carbide (C_γ), and
- crystalline, graphitic carbon (C_C).

2.2. Modeling of Deactivation Phenomena

From a mechanistic point of view, the coking process can be viewed as a consequence of the surface accumulation of carbon moieties due to a lower gasification rate relative to the accumulation rates of C_{alpha}, polymeric carbon and coke, by the CO decomposition (scheme 1a) or hexane cracking (scheme 1b).

Scheme 1. Carbon formation by CO decomposition (**a**) or hexane cracking (**b**).

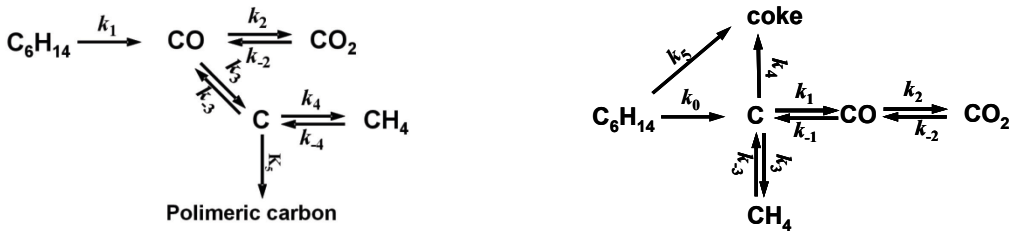

TEM pictures of the used catalyst samples in Figure 4 confirm that catalyst deactivation, feeding or not hydrogen, proceeds by different paths to form different inactive carbon or coke species. According to previous TGA results, under standard reaction conditions (run b) the catalyst grains (Figure 4B) appear embedded into an array of large carbon fibers (d_{fiber} = 20–50 nm), while no carbon deposits are apparent on the used catalyst in presence of H_2 (Figure 4C) [11,15,17,35], although halos surrounding several crystallites may be due to films of coke precursors.

Figure 4. TEM views (**A**–**C**) and PSD (**D**) of the "fresh" and "used" catalyst samples: (**A**) "fresh"; (**B**) "used" (run b); (**C**) "used" (run e); (**D**) CSD's of samples reproduced in panels A–C.

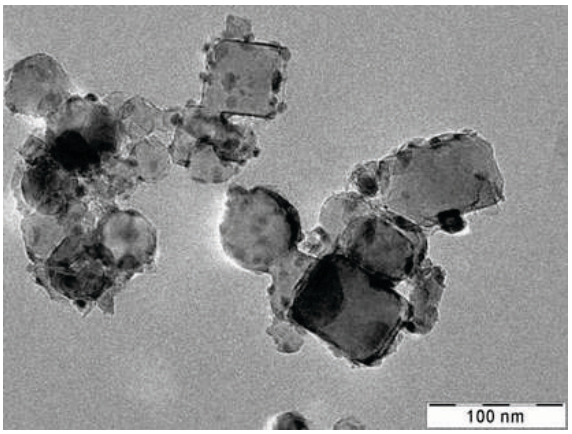

(**A**)

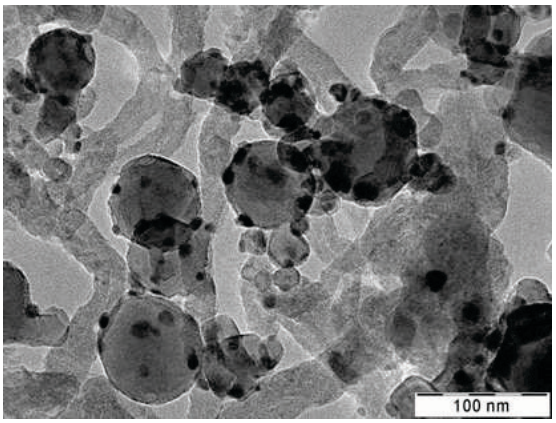

(**B**)

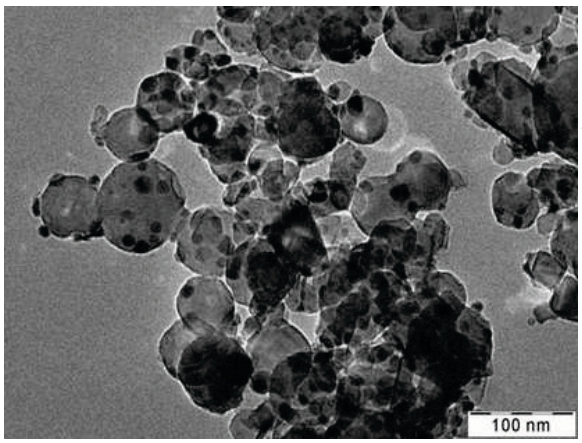

(**C**)

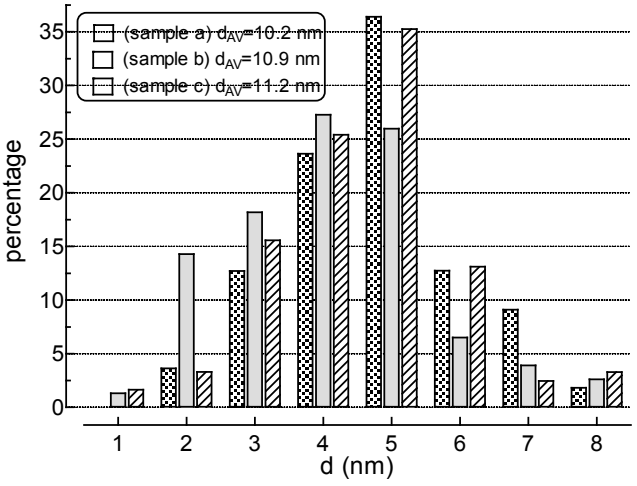

(**D**)

It should be emphasized that the principal cause of deactivation in prereforming or reforming of C_{2+} hydrocarbons at relatively low reaction temperatures is the formation of a hydrocarbonaceous film on the nickel surface [19] which poisons nickel sites. This work establishes that deactivation is minimized at high H_2 concentrations.

In both Runs b and e, an observed "smoothing" of the cubic habit of the magnesia carrier (Figure 4B,C) is consistent with moderate restructuring of the support, probably due to reaction with steam [15,16]; this is likely the origin of very modest metal sintering, apparent from minor changes in Ni crystallite size distributions (Figure 4D), accounting for *ca.* a 10% decrease in metal dispersion in agreement with H_2 uptake data [11].

As might be expected, thiophene co-feeding causes the most rapid decrease in reaction rate with a linear drop during the first 6 h, (Figure 2, run h) [7]. The amount of C_5H_5S fed during this time (0.05 g/kg hexane) corresponds to *ca.* 3 μmol (0.51 μmol/h), while the H_2 uptake of the fresh catalyst (120 μmol/g_{cat}) corresponds to a surface Ni atom concentration for a 0.025 g sample of 6.0 μmol (*i.e.*, 240 μmol/g_{cat} of surface Ni sites assuming a H/Ni adsorption stoichiometry of 1 [7,15]). Thus, during pre-reforming with the above specified feed of thiophene (run h), the maximum S/Ni surface atomic ratio (*i.e.*, average chemisorption stoichiometry) would be 0.5, assuming complete and irreversible adsorption of sulfur atoms, which is likely under these conditions; in other words, each thiophene molecule deactivates two Ni atoms. However, due to the rapid and irreversible adsorption of S atoms on surface Ni atoms, the rate of poisoning could be influenced by pore diffusional resistances; thus the amount of adsorbed S in the catalyst sample would drop off sharply at the front of the bed and the sharp interface of sulfur saturated nickel would travel slowly, similar to a chromatographic wave, through the catalyst bed. Hence, the equations modeling thiophene adsorption are very complex and by necessity would include expressions for diffusion into the pores, adsorption, dissociation, and the slowly moving axial concentration gradient through the bed, as illustrated by the sophisticated two-dimensional model of H_2S adsorption on a Ni steam reforming catalyst described by Rostrup-Nielsen [39].

From the previous discussion, the deactivation pattern of the Ni/MgO catalyst can be assessed taking into account the overall effects of coking, sintering, and poisoning. However, other than Run h, the behavior of deactivation *versus* time observed in Figures 2 and 5 is due primarily to the formation of carbon and coke, since negligible sulfur was present and effects of sintering were negligibly small. With the exception of Run h, in the presence of thiophene, deactivation was log-linear (see Figure 5), consistent with an exponential activity decay

$$\alpha = \exp[-k_{deact} \cdot t] \tag{9}$$

Accordingly, the first order deactivation rate equation is

$$-\frac{da}{dt} = k_{deact} \cdot a \quad \text{or} \quad -ln\alpha = k_{deact} \cdot t \tag{10}$$

These can be also expressed in terms of active sites availability (C_{site}), assuming that activity is directly proportional to the concentration of surface sites [20],

$$\alpha = \frac{C_{site}}{C_{site}^0} \tag{11}$$

and, thus

$$-\frac{dC_{site}}{dt} = k_{deact} \cdot C_{site} \quad \text{or} \quad -ln\left(\frac{C_{site}}{C^{0}_{site}}\right) = k_{deact} \cdot t \tag{12}$$

where C_{site} and $C°_{site}$ are the instantaneous and initial concentrations of active sites, respectively. Hence, the exponential decay of activity by coking is described by the equation

$$\alpha = e^{-(k_{cok})\cdot t} \tag{13}$$

which accounts for the general exponential-decay of catalytic activity for each of the runs in Figure 2. From the slopes of the linear fits of the deactivation rate data in Figure 5, the deactivation rate constants (k_{deact}) listed in Column 3 of Table 2 are obtained. It is further assumed that the rate of sintering (which depends mainly on temperature) is negligibly small for all runs given the very small change in crystallite diameter during reaction.

Figure 5. Plot of the relative activity at different experimental conditions (see Table 1) *vs.* t.o.s..

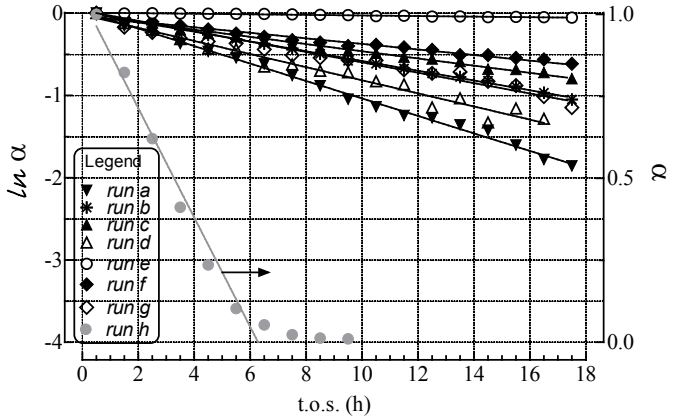

Table 2. Deactivation kinetic constants for coking.

Run	r^2	k_{cok} [a] (h^{-1})
a	1.00	$1.1 \times 10^{-1} \pm 2 \times 10^{-3}$
b	1.00	$5.5 \times 10^{-2} \pm 6 \times 10^{-4}$
c	0.99	$7.0 \times 10^{-2} \pm 1 \times 10^{-3}$
d	0.97	$7.7 \times 10^{-2} \pm 5 \times 10^{-3}$
e	0.96	-
f	0.98	$3.0 \times 10^{-2} \pm 1 \times 10^{-3}$
g	0.97	$6.3 \times 10^{-2} \pm 3 \times 10^{-3}$

a $k_{cok} = k_{deact}$.

It is emphasized that the calculation of rate constants in Table 2 (Run h involving sulfur poisoning excepted) relies on the following assumptions:

1 The rates of deactivation by coking and sintering are small relative to the rate of the main reaction. Hence the pseudo steady-state approximation can be made. This is a reasonable assumption in view of 2–3 orders of magnitude differences between reaction and coking rates at any condition and t.o.s. [15];

2 The rate of coking is slow enough that it is not influenced by a pore diffusional resistance for the deactivation process;

3 Pore diffusion resistance for the main reaction is neglected which, at high reaction rates and conversions, would lower the concentration of hydrocarbon coke precursors into the pores, then lowering coking rates along the pores; similarly concentration gradients through the bed due to high conversions should cause a decrease in adsorbed carbon concentration through the bed. This is probably a poor assumption in view of the high conversions of this study. Thus, the rate constants could be significantly in error due to differences in pore diffusional resistance between runs and represent at best rough averages across pellets and bed.

Figure 6. Log-plot of the kinetic constant of coking *vs.* water partial pressure (**A**); and Relationship between the weight gain of the used samples (Table 1) and the kinetic constant of coking (Table 2) at different reaction conditions (**B**).

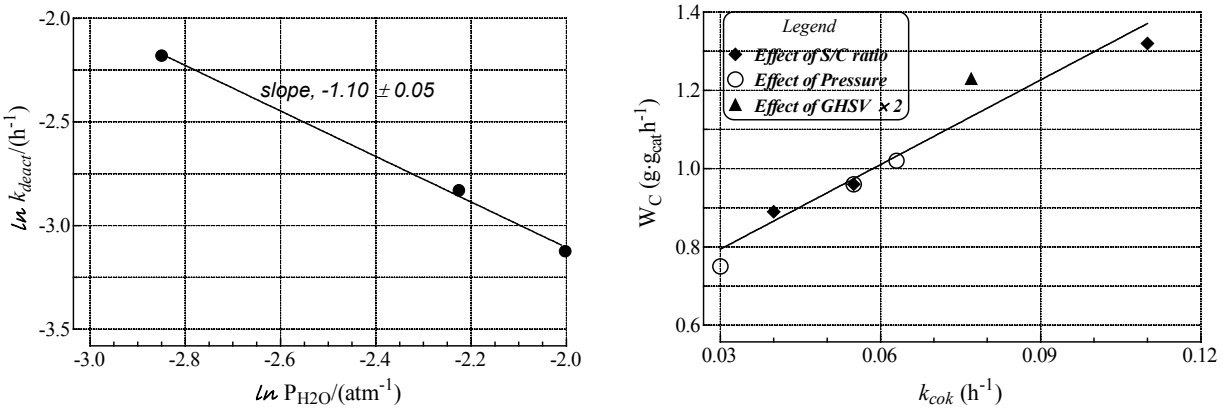

(**A**) (**B**)

Values of k_{cok} in Table 2 are not constant as predicted by the simple first order deactivation model; indeed, they vary by a factor of 20. In fact, the log-plot of k_{cok} (Figure 6A) discloses an inverse dependence (−1.10 ± 0.05) on P_{H2O}, confirming that water concentration is a key-factor in controlling coking rate at low H_2 concentrations (typical of steady-state), a logical result given that water is also a gasifying agent for carbon. The straight-line relationship between k_{cok} and weight gain in the used samples in Figure 6B supports a link between deactivation at low H_2 concentrations to fouling by C-deposits for a range of typical prereforming conditions.

2.3. Effect of Deactivation on Product Selectivity and Surface Functionalities

Thermodynamic and kinetic evaluations of the outlet stream composition [2,9,15,21–23] shed light on driving force for carbon deposition and, in turn, how carbon deposits influence selectivity. In particular, assuming hexane cracking to be irreversible [9,15,22], a rough estimate of the outlet stream composition can be made from a thermodynamic analysis of gasification (GAS), water-gas-shift (WGS), and methanation (MET) reactions (Table 3) [9–11,15]. However, also the Boudouard reaction has been considered to evaluate the incidence of CO dismutation on carbon formation and coking [11]. Specifically, P_x values obtained from conversion-selectivity data were substituted in the equilibrium

expressions to calculate experimental K_{exp} values of MET, GAS, WGS and DISP reactions as a function of t.o.s. [11].

Table 3. Thermodynamic constants of the various reactions of the steam reforming network (adapted from ref. [11] with the kind permission of Elsevier, copyright 2004).

Reaction	Stoichiometry			K_P [a]
CRK	C_6H_{14}	➞	6 C + 7 H_2	-
GAS	C + H_2O	⇆	CO + H_2	5.09×10^{-4}
WGS	CO + H_2O	⇆	CO_2 + H_2	7.47×10^{0}
MET	C + 2H_2	⇆	CH_4	5.41×10^{1}
DISP	2 CO	⇆	C + CO_2	1.47×10^{4}

Equilibrium pressure constant values at 450 °C with P_x values in MPa.

The ratio (β) of K_{exp} to the corresponding calculated value of the equilibrium constant K_{eq} at 450 °C (from Table 3) provides a measure of the distance from equilibrium for each reaction, allowing a reliable assessment of the effects of the S/C ratio (Figure 7A–C) and H_2 feeding (Figure 7D) on activity *versus* time patterns. Figure 7 shows that irrespective of t.o.s. and S/C ratio, the WGS reaction is always near thermodynamic equilibrium conditions, given that β_{WGS} values vary between 0.6 and 1.0. In contrast, gasification ($\beta_{GAS} \approx 0.5$) and, even more so, methanation (β_{MET}, 0.2–0.05) reactions operate far from equilibrium and are thus kinetically controlled. It follows from the previous discussion that lower rates of GAS and MET relative to hexane cracking constitutes a major driving force to carbon deposits build-up [17,19,20,35]. Furthermore, the observation that β_{DISP} is always larger than one implies a $[P_{CO2}/(P_{CO})^2]$ ratio greater than that allowed by thermodynamics, indicating that under prereforming conditions on Ni/MgO, the forward reaction, which also contributes to carbon formation, is more kinetically favorable than the reverse gasification of carbon by CO_2. However, this deviation could also be an artifact of the approximate reaction model.

It is interesting that while β_{GAS} and β_{MET} decrease with trends similar to that of the relative activity (α), β_{DISP} increases progressively with t.o.s. (almost exponentially under the conditions of Figure 7A), suggesting that carbon and coke reactivity decrease accordingly by ageing (*i.e.*, by conversion of coke precursors to highly polymerized coke and by conversion of $C_\alpha \rightarrow C_\beta$, C_V, C_γ, C_C) [16,17,19,21,36]. In fact, the changes in product selectivity with the activity level (Figure 3) mirror the different influences of coke and carbon on different functionalities of Ni catalysts, consistent with the ^{14}CO and $^{14}CO_2$ isotopic labeling experiments of Jackson *et al.* who found that Ni/Al_2O_3 catalyst retains high activity towards the scrambling of C-atoms and surface carbon gasification, despite a considerable decrease in the availability of metal surface area due to growth of gum-like carbonaceous deposits [35].

Figure 7. Pre-reforming of the *n*-hexane (*T*, 450 °C; *P*, 10 bar). Effect of S/C ratio and H_2 feeding on α and β values of GAS, WGS, MET and DISP reactions *vs.* t.o.s.: (**A**) S/C, 1.5; H_2/C, 0; (**B**) S/C, 2.8; H_2/C, 0; (**C**) S/C, 3.5; H_2/C, 0; (**D**) S/C, 2.8; H_2/C, 2. Legend: (●) α; (●) β_{WGS}; (○) β_{DISP}; (●) β_{GAS}; (●) β_{MET} (reproduced from ref. [11] with the kind permission of Elsevier, copyright 2004).

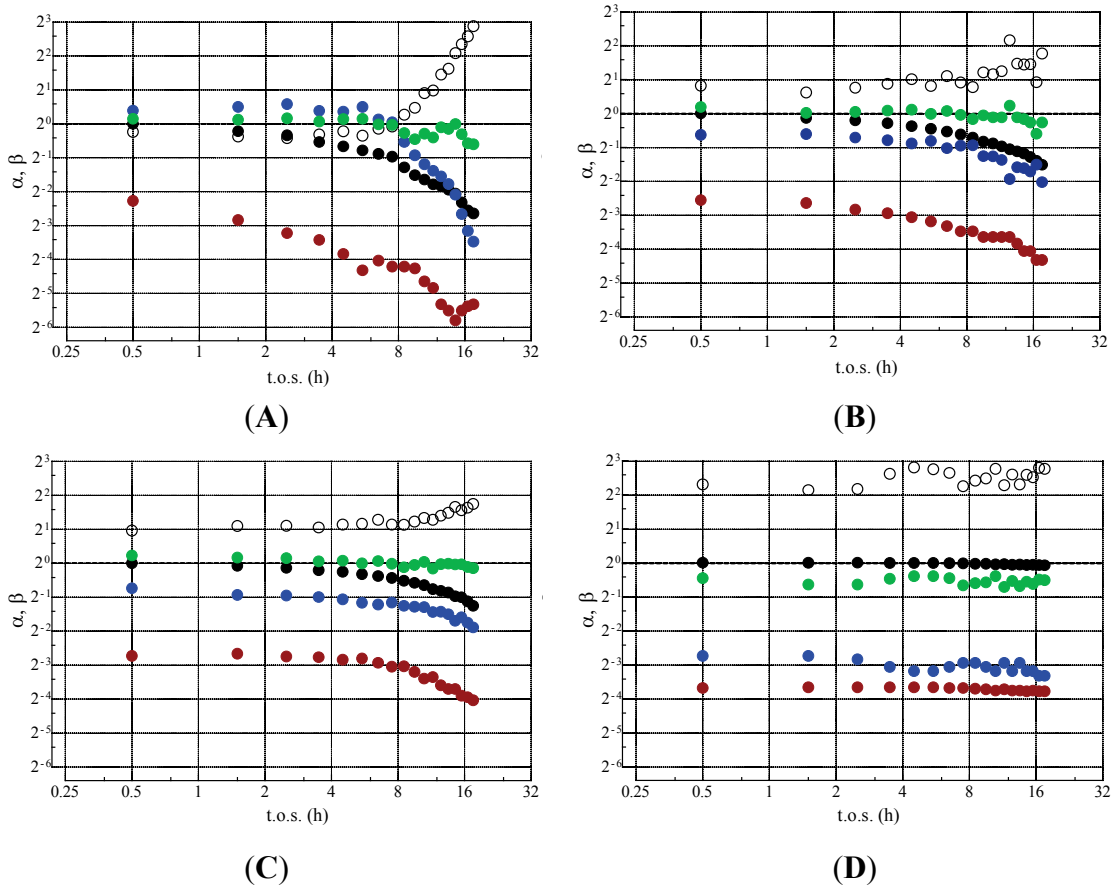

In the present paper, the role of the methanation reaction in modeling of prereforming has been emphasized. Bartholomew emphasized that methanation and steam reforming functionalities of Ni catalysts are closely related on the basis of the activation energy values [22]. Furthermore, Rostrup-Nielsen stressed that hydrogenolysis and steam reforming reactions share many surface steps, requiring also analogous ensembles (*n*, 2.5–2.7) of active sites [17]. Hence, effects of deactivation on prereforming catalyst functionalities can be assessed by inspecting the trends of the relative rates of MET, GAS, and WGS reactions ($\alpha_x = \alpha \cdot S_\chi$), as shown in Figure 8. The semi-log plot of the relative rates of CH_4 (α_{CH4}), CO (α_{CO}), and CO_2 (α_{CO2}) formation provides satisfactory linear trends (Figure 8), the slopes of which (k_{MET}, k_{GAS}, k_{WGS}) represent the decay constants for the above functionalities, listed in Table 4.

These figures reveal the following trends:

1. MET rate (α_{CH4}) decreases much more steeply than relative activity;
2. GAS rate (α_{CO}) decreases similar to relative activity;
3. WGS rate (α_{CO2}) decreases less than relative activity.

Figure 8. Relative rates of hexane conversion (α, ●), CH_4 (α_{CH4}, ▲), CO_2 (α_{CO2}, ◆) and CO (α_{CO}, ▼) formation *vs.* t.o.s. at different reaction conditions (see Table 1) (adapted from ref. [15] with the kind permission of Wiley, copyright 2006).

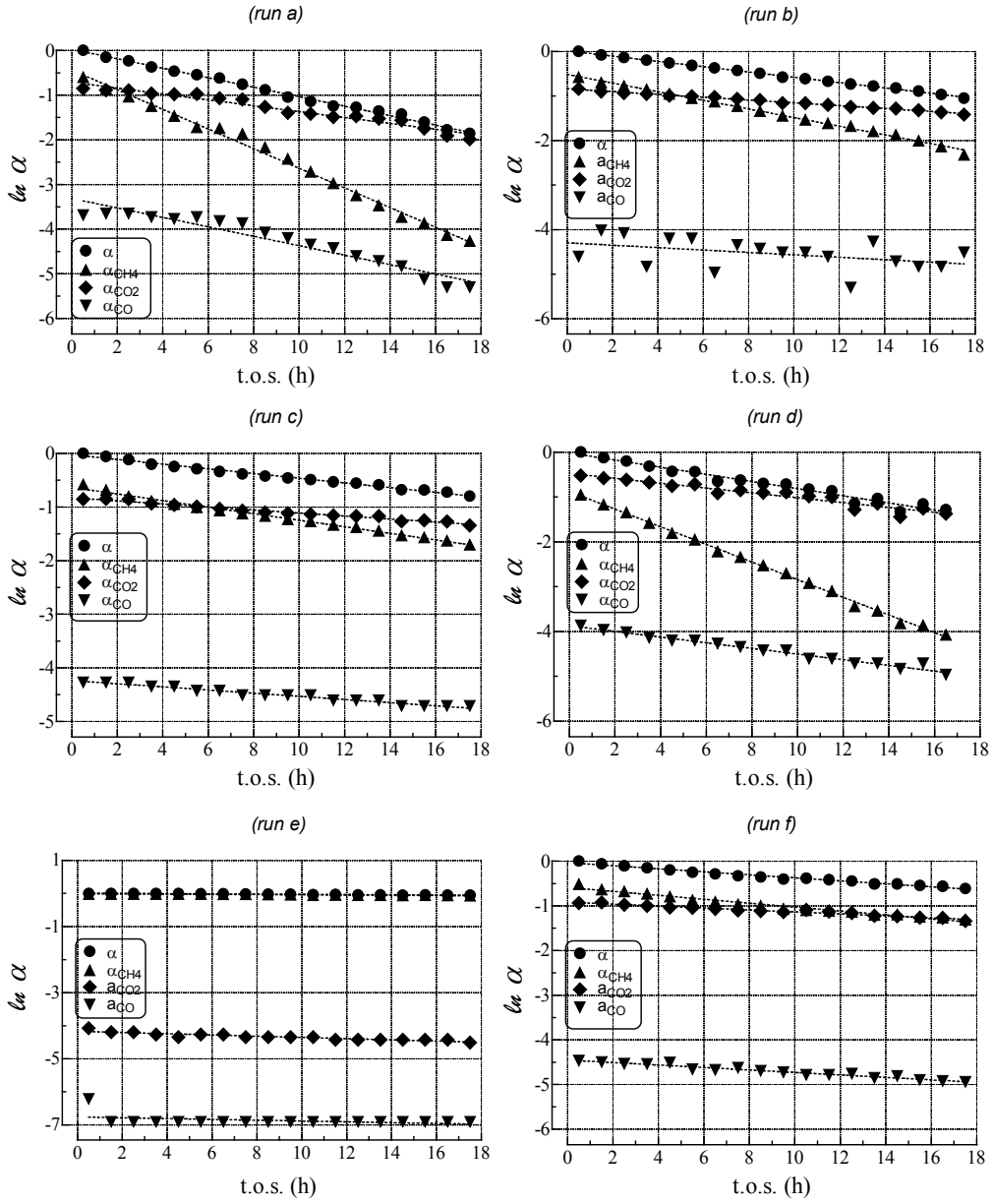

Indeed, direct relationships between k_{MET}, k_{GAS}, and k_{WGS} decay and that of activity loss (k_{deact}) result in straight-line correlations (Figure 9) with slopes equal to 2.7 ± 0.3, 1.1 ± 0.2 and 0.6 ± 0.1, respectively. From this and similar figures it can be shown that MET, GAS, and WGS functionalities depend on different *ensembles* of active sites [11,15,17,19–21,36]; thus, a slope of 1 for k_{GAS}/k_{deact} suggests that hexane conversion involves single sites leading to CO, while MET and WGS require larger and smaller ensemble of active sites for methane and carbon dioxide formation, respectively.

Table 4. Deactivation constants of the various functionalities (T, 450 °C): hexane conversion (k_{deact}), methanation (k_{MET}), gasification (k_{GAS}), water-gas-shift (k_{WGS}).

Run	k_{deact} [a] (h^{-1})	k_{cok} [a] (h^{-1})	k_{MET} (h^{-1})	k_{GAS} (h^{-1})	k_{WGS} (h^{-1})
a	1.1×10^{-1}	1.1×10^{-1}	2.2×10^{-1}	1.1×10^{-1}	6.6×10^{-2}
b	5.9×10^{-2}	5.6×10^{-2}	9.7×10^{-2}	2.7×10^{-2}	3.2×10^{-2}
c	4.4×10^{-2}	4.0×10^{-2}	6.0×10^{-2}	2.8×10^{-2}	2.7×10^{-2}
d	8.1×10^{-2}	7.7×10^{-2}	2.2×10^{-1}	7.1×10^{-2}	6.1×10^{-2}
e	3.5×10^{-3}	0.000	3.5×10^{-3}	1.2×10^{-2}	1.9×10^{-2}
f	3.4×10^{-2}	3.0×10^{-2}	4.4×10^{-2}	2.8×10^{-2}	2.2×10^{-2}

a data taken from Table 2.

In fact, according to Beeckman *et al.* who adopted a stochastic approach to describe deactivation by coking under different mechanisms [34], MET functionality is affected to the maximum extent by the fouling of active sites because of its high number of metal atoms required for each site (e.g., formal site molecularity) in comparison to GAS and WGS ones [11,15,17,19,40,41].

Therefore, in agreement with literature data, kinetic and thermodynamic findings confirm that surface carbon (*i.e.*, C_α) hydrogenation is the crucial step controlling activity, selectivity, and stability against coking in the pre-reforming process. Activity decay is more pronounced at low conversion, mostly under the occurrence of GAS and WGS reactions, as CO formation-decomposition is mainly responsible for carbon build-up *via* an adsorbed C_α intermediate [19,35].

Figure 9. Relationships between k_{MET} (●), k_{GAS} (▼), k_{WGS} (◆) and k_{deact} (*see* Table 4) (adapted from ref. [15] with the kind permission of Wiley, copyright 2006).

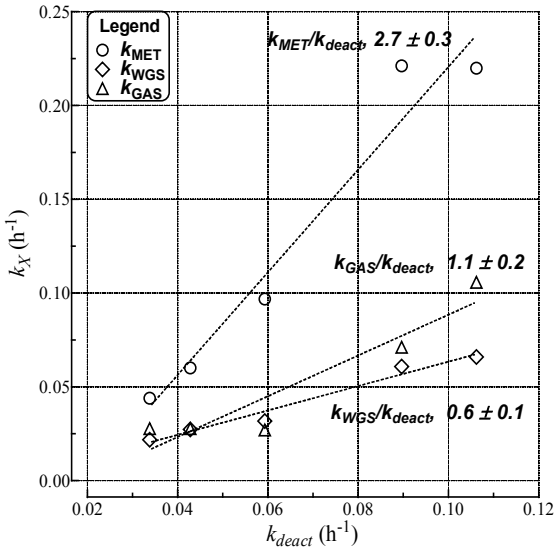

However, with addition of high concentrations of H_2, similar values of k_{deact} and k_{MET} (Table 4), and a much steeper decay of gasification ($k_{GAS}/k_{deact} \approx 3.5$) and WGS ($k_{WGS}/k_{deact} \approx 5$) functionalities [11,17,19] evidence that different reaction and deactivation paths are favored.

3. Experimental Section

3.1. Catalyst Preparation

The 19.1 wt% Ni/MgO catalyst was prepared by incipient wetness impregnation of "smoke" MgO powder (UBE Ltd., Yamaguchi, Japan SA_{BET}, 30 $m^2 \cdot g^{-1}$) with an ethanolic solution of the $Ni(NO_3)_2$ salt [28–31]. The catalyst was dried at 80 °C, calcined at 400 °C (16 h) and pre-reduced for 6 h at 650 °C under H_2 flow.

3.2. Catalyst Testing

Catalytic tests in the pre-reforming of n-hexane were performed at 450 °C and a pressure of 5–15 bar, using an isothermal "fixed bed" stainless steel microreactor (i.d., 6 mm), loaded with 25 mg of catalyst (40–70 mesh), diluted with same-sized SiC in a 1/30 weight ratio [11,15]. Before tests, the catalyst was heated at 450 °C and further reduced *in situ* for 1 h in H_2 flow (100 *STP* mL min^{-1}; *P*, 1 bar). The reaction mixture including *n*-C_6H_{14} (1.8%), N_2 (8.0%), H_2O (16.2–37.8%) and He (rest) for a variation of the S/C ratio between 1.5 and 3.5 respectively, was fed at the rate of 283 (GHSV, 12,000 h^{-1}) or 566 (GHSV, 24,000 h^{-1}) *STP* mL min^{-1}. The effects of H_2 (11.0%; H_2/C, 1.0) and thiophene (50 ppm in *n*-hexane) were probed at the highest GHSV and a S/C ratio of 2.8. Both water and n-hexane were fed as liquid by HPLC pumps. The reaction temperature was controlled by a thermocouple in contact with the catalytic bed, while the reactor stream was analyzed by a GC equipped with a three-columns analytical system connected to both TCD and FID detectors for permanent gases and hydrocarbons analyses, respectively [11,15].

3.3. Catalyst Characterization

TEM analyses were performed using a PHILIPS CM12 Transmission Electron Microscope (point-to-point resolution, 0.3 nm) on "fresh" and "spent" catalyst samples, dispersed ultrasonically in ethanol and deposited over a thin carbon film supported on a standard copper grid. The Ni particle size distribution (PSD) was obtained from an average of 150–200 particles, and the average volume-area particle size calculated by the conventional statistical formula [29–31]:

$$\bar{d}_{AV} = \frac{\sum_i n_i d_i^3}{\sum_i n_i d_i^2} \quad (1)$$

The H_2 uptake of "fresh" and "used" catalyst was evaluated by TPD measurements in the range −80–620 °C using Ar as carrier gas (30 *stp* $cm^3 \cdot min^{-1}$) after *in situ* reduction of the samples in H_2 flow at 450 °C for 1 h and subsequent saturation at r.t. (room temperature) and further at −80 °C. The fraction of reduced Ni was evaluated by titration at 450 °C with O_2 pulses ($Ni + ½\ O_2 \rightarrow NiO$) after TPD analysis [31].

TGA-DSC measurements of the "used" catalyst samples (5 mg) in the range of 20–400 °C were performed using a Simultaneous Thermal Analyser (STA 409C, Netzsch), operating in air with a heating rate of 10 °C/min and an accuracy of 0.01 mg.

4. Conclusions

This review summarizes highlights of previous studies (mainly in our laboratory) of reaction and deactivation paths on a "model" Ni/MgO catalyst in the pre-reforming of n-C_6H_{14} with steam at 450 °C. A kinetic and thermodynamic analysis of the data from these studies provides (1) new deactivation rate parameters for carbon deposition and coke formation and (2) insights into the surface reaction network of the pre-reforming process, including hexane cracking, water-gas-shift, and methanation reactions.

Important conclusions from this work can be summarized as follows:

- Deactivation of Ni/MgO by carbon deposition and coking follows a pseudo 1st-order dependence on active site concentration, consistent with an exponential decay with t.o.s. That deactivation by coke and carbon formation is not simple first order in site concentration, is evident from observed decreases in deactivation rate constants with increasing S/C ratio, P, and contact time.
- Comparison of thermodynamic predictions with experimental values of outlet stream composition leads to the conclusion that the kinetics of hexane cracking/reforming, carbon gasification and methanation reactions control the rate of coking; methanation is the critical, rate limiting step responsible for coke deposition in the near absence of H_2. Carbon formation via the Boudouard reaction is apparently thermodynamically and kinetically favored.
- Under simulated industrial pre-reforming conditions at a high H_2 concentration, hydrogen substantially increases reaction throughput by speeding up hydrogenolysis, CO formation via the water-gas-shift, and methanation reactions. H_2 at high concentrations gasifies coke and carbon precursors, thereby largely preventing formation of coke and inactive carbons.
- S-poisoning by thiophene co-feeding causes a sharp drop in catalytic activity due to irreversible poisoning; however, strong pore diffusional resistances in catalyst pellets and bed prevent an accurate analysis of the poisoning mechanism and kinetics.

Author Contributions

This work was conceived by Francesco Arena, who arranged the manuscript, and Giuseppe Trunfio, who carried out the experiments and also conceived and revised the manuscript.

Conflict of Interest

The authors declare no conflict of interest.

References

1. Piel, W.J. Transportation fuels of the future? *Fuel Process. Tech.* **2001**, *71*, 167–179.
2. Nagase, S.; Takami, S.; Hirayama, A.; Hirai, Y. Development of a high efficiency substitute natural gas production process. *Catal. Today* **1998**, *45*, 393–397.
3. Cromarty, B.J.; Hooper, C.W. Increasing the throughput of an existing hydrogen plant. *Int. J. Hydrogen Energy* **1997**, *22*, 17–22.

4. Aitani, A.M. Processes to enhance refinery-hydrogen production. *Int. J. Hydrogen Energy* **1996**, *21*, 267–271.
5. Fierro, J.L.G.; Peña, M.A.; Gómez, J.P. New catalytic routes for syngas and hydrogen production. *Appl. Catal. A* **1996**, *144*, 7–57.
6. Rostrup-Nielsen, J.; Christiansen, L.J. Concept in Syngas Manufacture. *Catalytic Science Series*; Imperial College Press: London, UK, 2011; Volume 10.
7. Bartholomew, C.H.; Farrauto, R.G. *Fundamental of Industrial Catalytic Processes*, 2nd ed.; J. Wiley & sons, Inc.: Hobken, NJ, USA, 2006; pp. 339–371.
8. Wang, X.; Gorte, R.J. A study of steam reforming of hydrocarbon fuels on Pd/ceria. *Appl. Catal. A* **2002**, *224*, 209–218.
9. Zou, X.; Wang, X.; Li, L.; Shen, K.; Lu, X.; Ding, W. Development of highly effective supported nickel catalysts for pre-reforming of liquefied petroleum gas under low steam to carbon molar ratios. *Int. J. Hydrogen Energy* **2010**, *35*, 12191–12200.
10. Shen, K.; Wang, X.; Zou, X.; Wang, X.; Lu, X.; Ding, W. Pre-reforming of liquefied petroleum gas over nickel catalysts supported on magnesium aluminum mixed oxides. *Int. J. Hydrogen Energy* **2011**, *36*, 4908–4916.
11. Arena, F.; Trunfio, G.; Alongi, E.; Branca, D.; Parmaliana, A. Modeling the activity-stability pattern of Ni/MgO catalysts in the pre-reforming of *n*-hexane. *Appl. Catal. A* **2004**, *266*, 155–162.
12. Ayabe, A.; Omoto, H.; Utaka, T.; Kikuchi, R.; Sasaki, K.; Teraoke, Y.; Educhi, K. Catalytic autothermal reforming of methane and propane over supported metal catalysts. *Appl. Catal. A* **2003**, *241*, 261–269.
13. Rostrup-Nielsen, J. Activity of nickel catalysts for steam reforming of hydrocarbons. *J. Catal.* **1973**, *31*, 173–181.
14. Rostrup-Nielsen, J. *Catalysis, Science and Technology*; Springer: Berlin, Germany, 1983.
15. Arena, F. Basic Relationships in the Pre-Reforming of *n*-Hexane on Ni/MgO Catalyst. *AIChE J.* **2006**, *52*, 2823–2831.
16. Christensen, T.S. Adiabatic prereforming of hydrocarbons—An important step in syngas production. *Appl. Catal. A* **1996**, *138*, 285–309.
17. Rostrup-Nielsen, J.; Alstrup, I. Innovation and science in the process industry: Steam reforming and hydrogenolysis. *Catal. Today* **1999**, *53*, 311–316.
18. Sperle, T.; Chen, D.; Lødeng, R.; Holmen, A. Pre-reforming of natural gas on a Ni catalyst. Criteria for carbon free operation. *Appl. Catal. A* **2005**, *282*, 195–204.
19. Bartholomew, C.H. Carbon deposition in methanation and steam reforming. *Catal. Rev. Sci. Eng.* **1982**, *24*, 67–112.
20. Butt, J.B.; Petersen, E.E. *Activation, Deactivation and Poisoning of Catalysts*; Academic Press: Inc.: San Diego, CA, USA, 1998.
21. Forzatti, P.; Lietti, L. Catalyst deactivation. *Catal. Today* **1999**, *52*, 165–181.
22. Bartholomew, C.H. Mechanism of catalyst deactivation. *Appl. Catal. A* **2001**; *212*, 17–60.
23. Kroll, V.C.H.; Swaan, H.M.; Mirodatos, C. Methane Reforming Reaction with Carbon Dioxide Over Ni/SiO_2 Catalyst. Deactivation Studies. *J. Catal.* **1996**, *161*, 409–422.
24. Tailleur, R.G.; Davila, Y. Optimal Hydrogen Production through Revamping a Naphtha-Reforming Unit: Catalyst Deactivation. *Energy Fuels* **2008**, *22*, 2892–2901.

25. Sehested, J.; Carlsson, A.; Janssens, T.V.W.; Hansen, P.L.; Datye, A.K. Sintering of nickel steam-reforming catalysts on $MgAl_2O_4$ spinel supports. *J. Catal.* **2001**, *197*, 200–209.
26. Ashrafi, M.; Pfeifer, C.; Pröll, T.; Hofbauer, H. Experimental Study of Model Biogas Catalytic Steam Reforming: 2. Impact of Sulfur on the Deactivation and Regeneration of Ni-Based Catalysts. *Energy Fuels* **2008**, *22*, 4190–4195.
27. Gallego, J.; Batiot-Dupeyrat, C.; Barrault, J.; Mondragón, F. Severe Deactivation of a $LaNiO_3$ Perovskite-Type Catalyst Precursor with H_2S during Methane Dry Reforming. *Energy Fuels* **2009**, *23*, 4883–4886.
28. Arena, F.; Parmaliana, A. Strategies of design of Ni/MgO catalysts for the reforming of hydrocarbon to hydrogen/syngas. *Curr. Top. Catal.* **2006**, *5*, 69–88.
29. Parmaliana, A.; Arena, F.; Frusteri, F.; Coluccia, S.; Marchese, L.; Martra, G.; Chuvilin, A. Magnesia Supported Nickel Catalysts. Part II: Surface properties and reactivity in CH_4 steam reforming. *J. Catal.* **1993**, *141*, 34–47.
30. Frusteri, F.; Spadaro, L.; Arena, F.; Chuvilin, A. TEM evidence for factors affecting the genesis of carbon species on bare and K-doped Ni/MgO catalysts during the dry-reforming of methane. *Carbon* **2002**, *40*, 1063–1070.
31. Arena, F.; Horrell, B.A.; Cocke, D.L.; Parmaliana, A.; Giordano, N. Magnesia-Supported Nickel Catalysts. I: Structure and morphological properties. *J. Catal.* **1991**, *132*, 58–67.
32. Suzuki, T.; Iwanami, H.; Yoshinari, T. Steam reforming of kerosene on Ru/Al_2O_3 catalyst to yield hydrogen. *Int. J. Hydrogen Energy* **2000**, *25*, 119–126.
33. Ming, Q.; Healey, T.; Allen, L.; Irving, P. Steam reforming of hydrocarbon fuels, *Catal. Today* **2002**, *77*, 51–64.
34. Beeckman, J.W.; Nam, I.-S.; Froment, G.F. Stochastic modeling of catalyst deactivation by site coverage. *Stud. Surf. Sci. Catal.* **1987**, *34*, 365–379.
35. Jackson, S.D.; Thomson, S.J.; Webb, G. Carbonaceous deposition associated with the catalytic steam-reforming of hydrocarbons over nickel alumina catalysts. *J. Catal.* **1981**, *70*, 249–263.
36. Snoeck, J.-W.; Froment, G.F.; Fowles, M.J. Filamentous carbon formation and gasification: thermodynamics, driving force, nucleation, and steady-state growth. *J. Catal.* **1997**, *169*, 240–249.
37. Chen, F.; Zha, S.; Dg, J.; Liu, M. Pre-reforming of propane for low-temperature SOFCs. *Solid State Ionics* **2004**, *166*, 269–273.
38. Sughrue, E.L.; Bartholomew, C.H. Kinetics of carbon monoxide methanation on nickel monolithic catalysts. *Appl. Catal.* **1982**, *2*, 239–256.
39. Rostrup-Nielsen, J. Sulfur Poisoning. In *Progress in Catalyst Deactivation*; Figuerido, J.L., Ed.; Martinus Nijhoff Publisher: The Hague, The Netherlands, 1982; pp. 209–227.
40. Sidjabat, O.; Trimm, D.L. Nickel-magnesia catalysts for the steam reforming of light hydrocarbons. *Top. Catal.* **2000**, *11/12*, 279–282.

41. Fujita, S.; Terenuma, H.; Nakamura, M.; Takezawa, N. Mechanisms of methanation of CO and CO_2 over Ni. *Ind. Eng. Chem. Res.* **1991**, *30*, 1146–1151.